ACS OMEGA

Article

Cite This: ACS Omega 2017, 2, 8010-8019

http://pubs.acs.org/journal/acsodf

Magnetic Sensing Potential of Fe_3O_4 Nanocubes Exceeds That of Fe_3O_4 Nanospheres

Arati G. Kolhatkar,[†] Yi-Ting Chen,[†] Pawilai Chinwangso,[†,‡] Ivan Nekrashevich,[‡] Gamage C. Dannangoda,[§] Ankit Singh,[∥] Andrew C. Jamison,[†] Oussama Zenasni,[†] Irene A. Rusakova,[⊥] Karen S. Martirosyan,*[,§] Dmitri Litvinov,*[,†,‡,∥] Shoujun Xu,*[,†] Richard C. Willson,*[,∥] and T. Randall Lee*[,†]

[†]Department of Chemistry and Texas Center for Superconductivity, [‡]Department of Electrical and Computer Engineering, [∥]Department of Chemical and Biomolecular Engineering, and [⊥]Department of Physics and Texas Center for Superconductivity, University of Houston, 4800 Calhoun Road, Houston, Texas 77204, United States

[§]Department of Physics, University of Texas Rio Grande Valley, Brownsville, Texas 78520, United States

Supporting Information

ABSTRACT: This paper highlights the relation between the shape of iron oxide (Fe_3O_4) particles and their magnetic sensing ability. We synthesized Fe_3O_4 nanocubes and nanospheres having tunable sizes via solvothermal and thermal decomposition synthesis reactions, respectively, to obtain samples in which the volumes and body diagonals/diameters were equivalent. Vibrating sample magnetometry (VSM) data showed that the saturation magnetization (M_s) and coercivity of 100−225 nm cubic magnetic nanoparticles (MNPs) were, respectively, 1.4−3.0 and 1.1−8.4 times those of spherical MNPs on a same-volume and same-body diagonal/diameter basis. The Curie temperature for the cubic Fe_3O_4 MNPs for each size was also higher than that of the corresponding spherical MNPs; furthermore, the cubic Fe_3O_4 MNPs were more crystalline than the corresponding spherical MNPs. For applications relying on both higher contact area and enhanced magnetic properties, higher-M_s Fe_3O_4 nanocubes offer distinct advantages over Fe_3O_4 nanospheres of the same-volume or same-body diagonal/diameter. We evaluated the sensing potential of our synthesized MNPs using giant magnetoresistive (GMR) sensing and force-induced remnant magnetization spectroscopy (FIRMS). Preliminary data obtained by GMR sensing confirmed that the nanocubes exhibited a distinct sensitivity advantage over the nanospheres. Similarly, FIRMS data showed that when subjected to the same force at the same initial concentration, a greater number of nanocubes remained bound to the sensor surface because of higher surface contact area. Because greater binding and higher M_s translate to stronger signal and better analytical sensitivity, nanocubes are an attractive alternative to nanospheres in sensing applications.

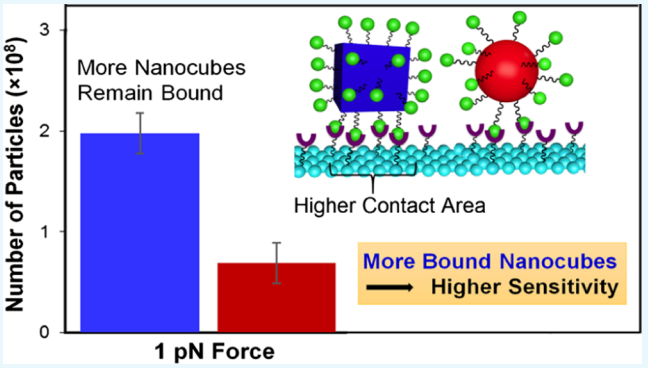

INTRODUCTION

Magnetic nanoparticles (MNPs) find widespread use in biomedical applications.[1−6] Although there have been significant advances in understanding the relation between nanoparticle structure and the corresponding magnetic properties,[7] tuning the properties of MNPs is complicated by the interdependent influences of various factors on magnetic properties. A recent review has summarized the parameters (size, shape, composition, and shell−core design) that can be modulated to tailor the properties for a particular application.[8] Extensive data exist on the effects of size,[9−11] composition,[12−14] and core−shell design;[15−17] however, efforts to understand the effect of shape on magnetic properties are comparatively rare and largely inconclusive.

There have been efforts to synthesize MNPs of various shapes: ferrite nanocubes,[18−20] maghemite nanorods,[21] NiFe nanowires,[22] cobalt nanodiscs,[23,24] magnetite tetrapods,[2] and Au−MnO nanoflowers,[25] and there is some literature on the influence of the particle shape on magnetic properties.[11,19,26−32] However, only a handful of studies,[29−32] which are summarized in Table S1 in the Supporting Information, have focused on comparing the magnetic properties as a *function of shape* using a common basis (same volume or same diameter/body diagonal). Further, the shape of MNPs has been shown to play an important role during particle adhesion, distribution, and internalization in biosensing or drug delivery.[33] However, can the correlation between shape and magnetization or sensing potential be attributed simply to geometry?

Received: September 5, 2017
Accepted: October 19, 2017
Published: November 16, 2017

DOI: 10.1021/acsomega.7b01312
ACS Omega 2017, 2, 8010−8019

The effect of geometry on magnetic properties has been evaluated for drug-delivery applications;[34,35] however, research that compares nanoparticles of different shapes based on their sensing ability is sorely lacking. Drug delivery relies on the ability of the nanoparticles to reach the diseased cells through the circulatory system and then adhere to those cells. Adhesion efficiency can be maximized by controlling the size, shape, and surface functionalization of nanoparticles.[36] Using computational modeling, Gao and co-workers noted that the tumbling motion of nanorods as compared to the rolling motion of nanospheres and the inherent high contact area of nanorods when they are parallel to the cell surface contributed significantly toward enhanced contact and binding to vascular walls.[36] Multiple studies by Decuzzi, Ferrari, and co-workers reported a higher adhesion probability for an ellipsoidal nanoparticle because of its larger surface area available for contact as compared to a spherical nanoparticle of the same volume.[34,37,38] Recently, Ferrari and co-workers have focused on nanoparticle design considerations that would overcome the barriers to drug delivery and have concluded the importance of shape in strong adhesion to facilitate drug delivery.[39] We hypothesized that the advantage of more contact points and higher binding using nonspherical geometries can be extended to sensing applications. For sensing, the larger contact area of cubic nanoparticles can lead to a more robust binding to a sensing platform or cell surface. Correspondingly, cubic Fe_3O_4 nanoparticles have a higher surface area available for contact with a planar interface as compared to spherical Fe_3O_4 nanoparticles (Scheme 1), and can thus adhere more strongly

Scheme 1. Contact Area for Spherical MNPs Compared to Cubic MNPs

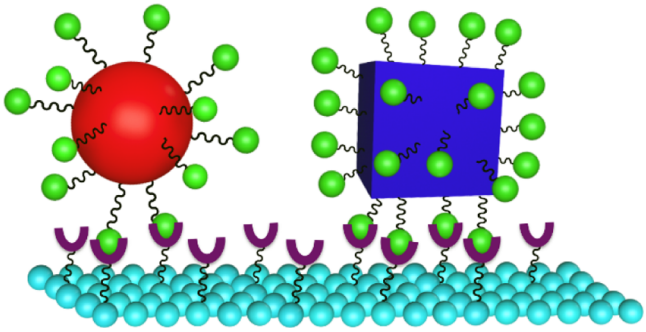

to a sensing platform. The increased adhesion should offer enhanced sensitivity and improved signal-to-noise ratios for cubic MNPs. To take advantage of this benefit, the design of cubic nanoparticles should ensure that the high-contact-area geometry is retained after coating/functionalization. Separately, a recent study that focused on retaining the cubic shape after coating the particles with silica showed that, even after functionalization, the advantage of the higher surface contact area could be harnessed.[40]

Prior studies that explored the influence of the nanoparticle shape on magnetic properties primarily focused on particles with diameters less than 25 nm (Table S1).[29−32] Furthermore, the results from these studies showed no conclusive evidence on which shape corresponded to optimum magnetic properties. When comparing a set of same magnetization $CoFe_2O_4$ cubes and spheres, Song and Zhang[29] attributed lower coercivity for cubic nanoparticles to diminished surface pinning, which is a consequence of fewer missing coordinating oxygen atoms in the cubic nanoparticles compared to the spherical nanoparticles. The Noh group rationalized the higher M_s in cubic nanoparticles as compared to spherical nanoparticles of the same volume by simulating the orientations of the magnetic spin structures using an object-oriented micromagnetic framework program. These researchers found that the disordered spins were 4% in cubic MNPs and 8% in spherical MNPs.[41] On the basis of these simulations, the authors hypothesized that the lower percentage of disordered spins in 18 nm edge $Zn_{0.4}Fe_{2.6}O_4$ nanocubes gave rise to a higher M_s as compared to 22 nm diameter nanospheres of equivalent volume. An earlier study observed significantly higher blocking temperatures (T_B) for 14 nm spheres of γ-Fe_2O_3 as compared to 12 nm edge nanocubes of the same composition.[30] Because T_B is directly proportional to the effective anisotropy (for such small MNPs, surface anisotropy dominates the bulk anisotropy), the authors ascribed the higher T_B of spherical nanoparticles to their larger surface disorder and higher surface anisotropy.[30] In contrast to the results reported by the Song and Noh groups,[29,41] γ-Fe_2O_3 nanocubes with lower surface anisotropy showed higher coercivity but roughly the same saturation magnetization as the spherical MNPs.[30] In separate studies, Zhen et al. observed higher saturation magnetization (M_s) for cubic iron oxide MNPs as compared to spherical iron oxide MNPs of the same volume and attributed the difference to the higher crystallinity in cubic nanoparticles despite using the same method of synthesis (thermal decomposition).[31] Similarly, some researchers have noted a linear relationship between magnetization and crystallinity, observing an improvement in magnetic properties with higher crystallinity for lithium-, cobalt-, zinc-, and copper-ferrite nanoparticles.[42−45]

On the whole, while many studies have touted the superior magnetic properties of cubic MNPs, the summary presented here illustrates a lack of consensus regarding the phenomenon (or phenomena) underpinning the superiority. To this end, the studies reported here attempt to provide a more definitive perspective by examining two systematically prepared series of Fe_3O_4 nanocubes and nanospheres in which (1) the particle volumes and (2) the body diagonals/diameters are equivalent. Additionally, we use high-resolution transmission electron microscopy (TEM) and X-ray diffractometry (XRD) to evaluate the particle crystallinity.

The size range at which MNPs are classified as superparamagnetic, single-domain, or multidomain depends not only on the size, but also on the chemical composition of the nanoparticles; Fe_3O_4 MNPs are superparamagnetic when smaller than ∼25 nm, single-domain at 25−80 nm, and multidomain beyond 80 nm.[8,45] Most of the shape-comparative studies have been performed for MNP sizes that fall within the superparamagnetic regime[46] or at least in the single-domain regime.[46] For sensing applications, however, larger nanoparticles exhibit higher magnetization and are thus preferred for signal amplification considerations. Consequently, for the analysis presented in this paper, we explored the multidomain size range for the comparison of cubic (body diagonals of 135, 150, 175, and 225 nm) and spherical (diameters of 100, 125, 135, 150, 175, and 225 nm) Fe_3O_4 MNPs to focus on the effect of shape on the magnetic properties and sensing potential of MNPs. More specifically, we chose to focus our studies on magnetite nanoparticles in the multidomain size range based on (1) the relative ease of synthesis of these iron oxide nanoparticles, (2) their established utility in sensing applications, and (3) the notable absence of a systematic comparison

DOI: 10.1021/acsomega.7b01312
ACS Omega 2017, 2, 8010−8019

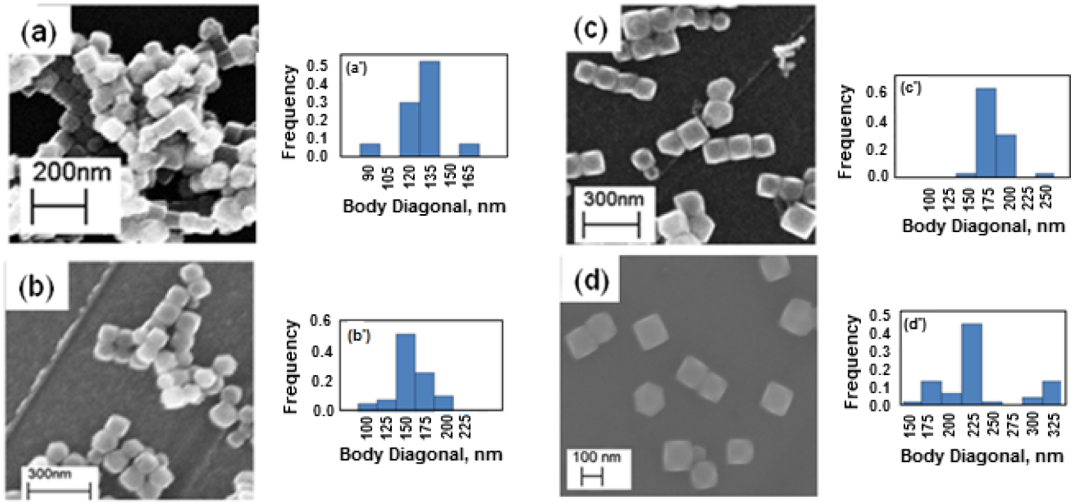

Figure 1. (a–d): SEM images of cubic Fe_3O_4 nanoparticles having body-diagonal lengths of 135, 150, 175, and 225 nm. (a′–d′): Corresponding size distributions.

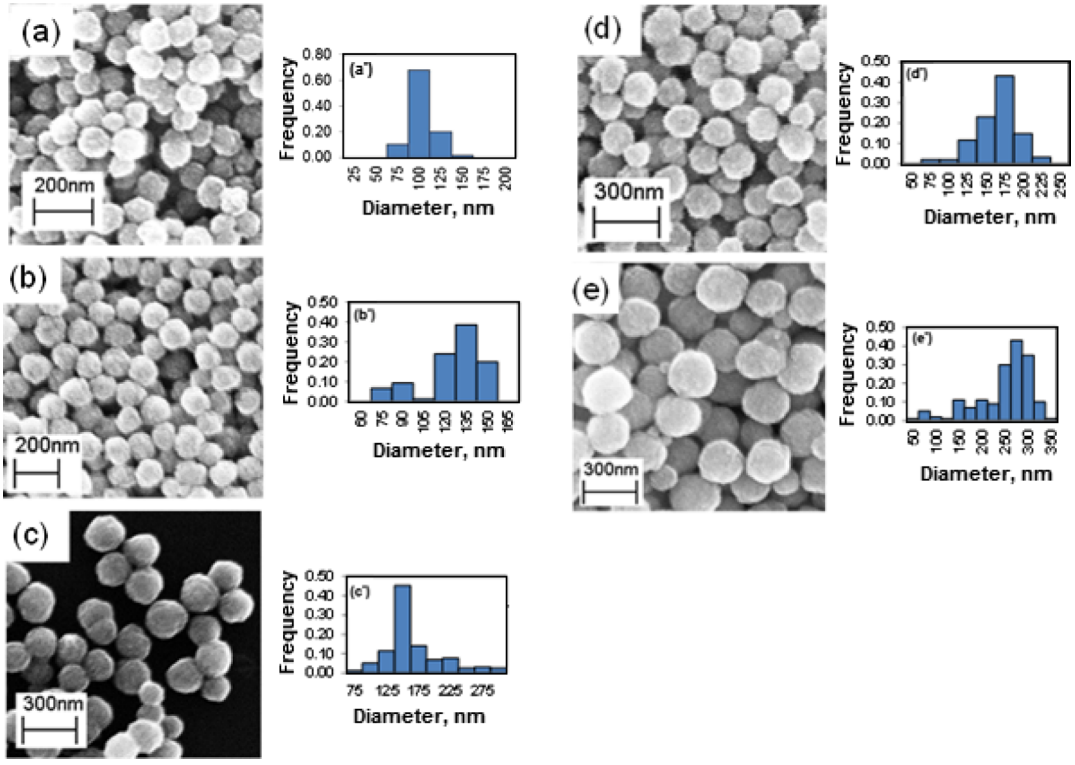

Figure 2. (a–e): SEM images of spherical Fe_3O_4 nanoparticles of diameters (a) 100, (b) 125, (c) 135, (d) 150, (e) 175, and (f) 275 nm. (a′–e′): Size distributions of nanoparticles shown in images a–e.

of the magnetic properties of cubic and spherical Fe_3O_4 nanoparticles, particularly in this size regime.

RESULTS AND DISCUSSION

Using the synthetic method reported by Kim et al.[20] that afforded magnetite nanocubes having body-diagonal lengths of 35–275 nm (~20–160 nm side length), we prepared oleic acid-stabilized Fe_3O_4 nanocubes having body-diagonal lengths in the range 135–225 nm by controlling the reaction time and agitation. Similarly, we modified the reaction time and agitation in a method developed by Deng et al.[47] to obtain Fe_3O_4 nanospheres with diameters in the size range of 100–275 nm.

Figures 1 and 2 show the scanning electron microscopy (SEM) images for the resulting series of nanocubes and nanospheres, and the associated size distributions. From the SEM images, we determined that the average sizes and the relative standard deviation (SD) values for the diameters of the spherical Fe_3O_4 MNPs were 100 ± 9, 135 ± 18, 150 ± 17, 175 ± 19, and 275 ± 17 nm, and those for the body diagonals of the cubic Fe_3O_4 MNPs were 135 ± 12, 150 ± 14, 175 ± 19, and 225 ± 20 nm.

For particles having the same-body diagonal/diameter, nanocubes and nanospheres of 135, 150, and 175 nm were compared. Separately, comparison of the same-volume pairs included nanocubes of 150, 175, and 225 nm body-diagonal lengths and nanospheres of 100, 125, and 150 nm diameters,

DOI: 10.1021/acsomega.7b01312
ACS Omega 2017, 2, 8010–8019

respectively. The magnetic properties, saturation magnetization (M_s), and coercivity (H) were obtained for each sample using vibrating sample magnetometry (VSM). Both shapes exhibited ferrimagnetic behavior. We have summarized the saturation magnetization and coercivity data for the synthesized nanocubes and nanospheres in Table 1. Tables 2 and 3 highlight a

Table 1. Magnetic Properties of Cubic and Spherical Fe_3O_4 MNPs as a Function of MNP Size[a]

MNP shape	size (nm)	M_s (emu/g)	H (G)
cube	135	90	139
	150	95	165
	175	95	177
	225	80	80
sphere	100	69	106
	135	72	42
	150	65	66
	175	32	21
	275	56	28

[a]Size refers to the body diagonal of nanocubes and the diameter of nanospheres.

Table 2. Magnetic Properties of Fe_3O_4 Nanocubes and Nanospheres Having the Same-Body Diagonal/Diameter

MNP shape	size (nm)	M_s ratio[a]	H ratio[b]
cube	135	1.3	3.3
sphere	135		
cube	150	1.5	2.1
sphere	150		
cube	175	3.0	8.4
sphere	175		

[a]M_s ratio = $(M_s)_{nanocubes}/(M_s)_{nanospheres}$. [b]$H$ ratio = $(H)_{nanocubes}/(H)_{nanospheres}$.

Table 3. Magnetic Properties of Fe_3O_4 Nanocubes and Nanospheres Having the Same Volume

MNP shape	size (nm)	M_s ratio[a]	H ratio[b]
cube	150	1.4	1.6
sphere	100		
cube	175	1.4	1.7
sphere	125		
cube	225	1.2	1.2
sphere	150		

[a]M_s ratio = $(M_s)_{nanocubes}/(M_s)_{nanospheres}$. [b]$H$ ratio = $(H)_{nanocubes}/(H)_{nanospheres}$.

comparison of the properties on a same-volume and same-body diagonal/diameter basis. For nanospheres in the 100−275 nm size range, the average M_s of the particles was 60 ± 15 emu/g. However, nanocubes in the 125−225 nm size range displayed an average M_s of 90 ± 7 emu/g. Overall, cubic Fe_3O_4 MNPs showed higher saturation and coercivity values than matched spherical Fe_3O_4 MNPs.

We further characterized these nanoparticles using TEM. Figure 3 shows images of a representative pair of same-volume MNPs and a representative pair of same-body diagonal/diameter MNPs. The images reveal that the nanocubes (a,c) are highly crystalline and the nanospheres (b,d) are polycrystalline.

To develop quantitative data for the degree of crystallinity for these samples, we evaluated and compared the XRD patterns of

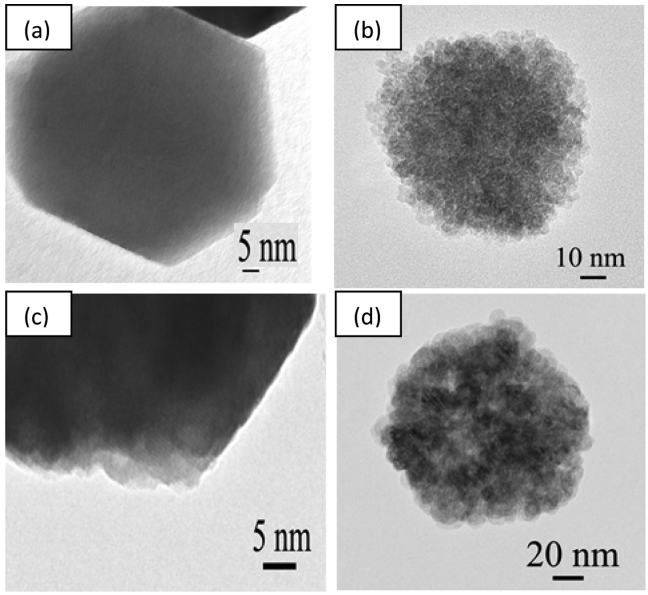

Figure 3. TEM images of (a) 150 nm cubic Fe_3O_4 MNPs, (b) 100 nm spherical Fe_3O_4 MNPs, (c) 135 nm cubic Fe_3O_4 MNPs, and (d) 135 nm spherical Fe_3O_4 MNPs.

the cubic and spherical Fe_3O_4 MNPs. Figure 4 shows that the cubic MNPs exhibited much sharper peaks as compared to the broad peaks associated with the spherical MNPs. To evaluate the crystallinity of the MNPs on a quantitative basis, we calculated the crystallite size. This parameter is inversely proportional to the peak width based upon Scherrer's formula, as shown in eq 1.[48]

$$\text{Crystallite size} = (K \times \lambda)/(\beta \cos 2\theta) \quad (1)$$

where K = shape factor. λ = wavelength (0.154 nm). β = line broadening at 1/2 the maximum intensity (rad). θ = Bragg angle.

The broad peaks of the spherical MNPs as compared to the sharp peaks for the cubic MNPs indicate that the crystallite size of the cubic sample is larger. We calculated the crystallinity index (CI) value for the nanocubes and nanospheres using eq 2.[49]

$$\text{CI} = [(\text{MNP size by SEM/TEM})/(\text{crystallite size})] \quad (2)$$

Table 4 lists the crystallite size and the CI of one representative pair each of the same-volume and same-body diagonal/diameter Fe_3O_4 MNPs. We provide additional data for a wide range of crystallite sizes as the Supporting Information (see Table S2). Please note that a lower CI value by definition corresponds to a higher degree of crystallinity (i.e., a CI of 1 indicates a crystal that is completely monocrystalline).[49] On the whole, the XRD data complement the TEM images, where results of both analyses show that cubic Fe_3O_4 MNPs had a higher degree of crystallinity as compared to spherical Fe_3O_4 MNPs.

We propose that the higher saturation magnetization observed for the nanocubes (see Tables 1−3) is due to their greater crystallinity. Previous studies have shown that the high crystallite size in nanocubes leads to high saturation magnetization because of reduced surface spin disorder.[13,31,50] Liu et al. varied the crystal size and showed that for polycrystalline nanospheres less than 250 nm in size, the saturation magnetization depends on both the diameter and its crystal

DOI: 10.1021/acsomega.7b01312
ACS Omega 2017, 2, 8010−8019

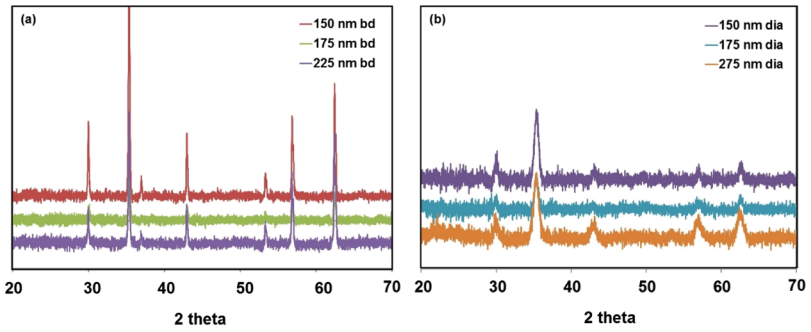

Figure 4. XRD patterns for Fe_3O_4 (a) nanocubes and (b) nanospheres.

Table 4. Crystallite Size and the CI for the Fe_3O_4 Nanocubes and Nanospheres Shown in Figure 3

MNP shape	size (nm)	basis	crystallite size (nm)	CI
cube	150	same-volume	56	4
sphere	100		17	6
cube	175	same-body diagonal/diameter	43	4
sphere	175		12	15

size (and hence crystallinity).[50] As expected,[50,51] owing to the higher crystal size in the multidomain MNPs, the saturation magnetization of Fe_3O_4 nanocubes is higher than that of nanospheres (Tables 1−3).

To compare the magnetic properties of nanocubes and nanospheres on the basis of same crystallinity, we attempted to generate spherical MNPs (>100 nm) with a higher degree of crystallinity by varying the surfactant (oleic acid) concentration using the solvothermal method and by carrying out liquid reduction synthesis at higher temperatures (up to 290 °C). However, these efforts have thus far been unsuccessful. Additionally, we measured the Curie temperature (T_C) of these spherical and cubic MNPs, and the results are shown in Figure 5. In the size range studied, the overall T_C for cubic MNPs is greater than that of spherical MNPs. The Curie temperature identifies the transition point from ferrimagnetic (in case of Fe_3O_4 MNPs) to paramagnetic. Because the Curie temperature for both types of our MNPs is quite high (780−840 K range), our data simply serve as another parameter of comparison.

After characterizing the MNPs (cubic and spherical), we evaluated the potential use of these MNPs in a sensing application and investigated their response using giant magnetoresistance (GMR) sensing and force-induced remnant magnetization spectroscopy (FIRMS). We compared the effectiveness of cubic and spherical MNPs as reporters of biomolecular agents (targets) using our in-house-built GMR biosensor. Since its first report by Baselt et al.,[52] several groups have continued the research and development of magnetic biosensing technology.[53−61] The biodetection scheme employs MNPs as reporters of biological agents, which are detected using a magnetoresistive element, where the resistance of the magnetoresistive sensor changes in the presence of MNPs. The GMR effect is the consequence of spin-polarized electron transport in GMR multilayer structures such as the Co/Cu/Co multilayers used in this work.[62−66] The resistance of GMR magnetic field sensors depends on the mutual orientation of Co magnetic layers in the Co/Cu/Co multilayer. When the magnetization directions of the ferromagnetic Co layers are aligned in the same direction, the structure/sensor is in its low resistance state. When the magnetization of the Co layers is antiparallel, the sensor exhibits high resistance.

A GMR sensor detects stray fields generated by MNPs placed in the vicinity of the sensor. Experimentally, the presence of MNPs is manifested by the modification of the dependence of the sensor resistance on the applied external magnetic field as shown in Figure 6. Because of the hysteretic behavior of the material, there are two high-resistance states, both symmetrically offset from zero. The positions of the resistance maxima (peaks) in these GMR curves shift in the presence of MNPs. Δx is estimated as the difference in peak-to-peak distance in the absence and presence of MNPs. Here, approximately 4.9×10^{10} MNPs were deposited on the GMR sensor, and the change in peak-to-peak distance (Δx) was recorded. Figure 6 shows the magnetoresistance curve (and Δx) of 135 nm cubic Fe_3O_4 MNPs on one representative sensor, illustrating the dependence of the GMR sensor resistance on the magnetic field in the absence and presence of MNPs.

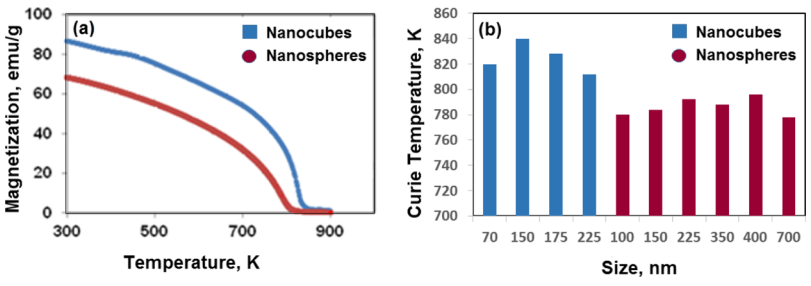

Figure 5. (a) Magnetization as a function of temperature for one pair of same diameter/body diagonal spherical/cubic MNPs and (b) Curie temperatures of spherical and cubic nanoparticles as a function of size.

DOI: 10.1021/acsomega.7b01312
ACS Omega 2017, 2, 8010−8019

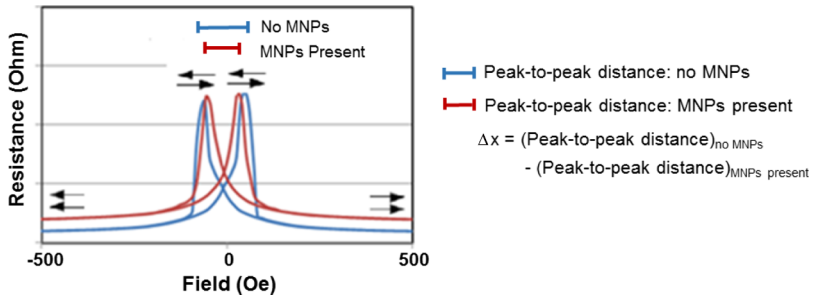

Figure 6. Plot of a typical response of a GMR sensor in the absence and presence of MNPs. The arrows indicate the corresponding magnetization states.[67] The representative data shown are for 135 nm cubic Fe_3O_4 on one sensor.

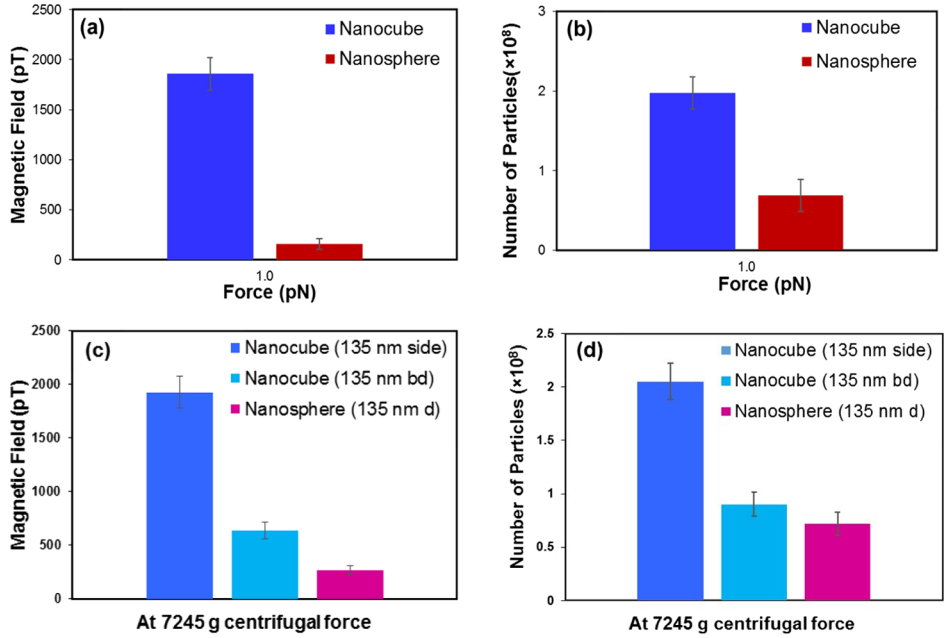

Figure 7. (a) Magnetization profiles in pico-Tesla vs centrifugal force in pico-Newton for nanocubes and nanospheres of the same volume. (b) Number of particles on the sensor at 1 pN. (c) Magnetization profiles for nanocubes and nanospheres of 135 nm [side length (side), body diagonal (bd), and diameter (d)] and (d) number of particles on the sensor after centrifugation at 7245*g* centrifugal force. Initial numbers of particles are stated in the text.

For cubic MNPs, Δx was ~18 ± 9 Oe and was observed to be higher than the ~4 ± 4 Oe obtained for spherical MNPs of the same volume. Data from five sensors were used to calculate the average in each case. The experiment was carried out with the same particle count for both cubic and spherical MNPs (see the Experimental Section), and although it is likely that the cubic shape improves sensor surface contact, we were unable to determine quantitatively the relative coverage on each sensor.

To highlight the advantage of a higher contact area and overcome the concern of nonspecific binding, we functionalized these nanoparticles with biotin and used the FIRMS technique to demonstrate how strongly these particles bind to the streptavidin-functionalized surface when subjected to varying centrifugal forces.[68,69] Notably, FIRMS uses an atomic magnetometer to measure the magnetization of ligand-conjugated magnetic particles as a function of an external force. In this study, biotin serves as the molecule to be detected and is the ligand attached to the MNPs. When the biotin-functionalized MNPs come in contact with the streptavidin-conjugated surface, the MNPs bind to the surface. When force is applied, the nonspecifically bound MNPs are removed from the surface. In the FIRMS technique employed here, the unbound nanoparticles are removed from the surface at high centrifuge speeds (strong centrifugal force).

Figure 7 shows the FIRMS results for biotin-functionalized particles on the streptavidin surface. The magnetization on the *y*-axis reflects the number of nanoparticles that are present on the surface. At strong (1 pN) forces, the magnetization response of the nanocubes that remained on the surface was higher than that of the same-volume nanospheres (see Figures 7a and 7b). The difference of the magnetic response on the streptavidin surfaces can be explained by comparing the (1) magnetic strength of nanocubes to that of nanospheres and (2) the surface area of nanocubes to that of nanospheres. Figure S1 shows the magnetic calibration curves versus the mass concentration, measured using an atomic magnetometer. The magnetic calibration curves based on the same mass for the same volume of MNPs display a linear trend, where nanocubes show higher magnetic strength than nanospheres. The *y*-axis in Figure 7b reflects the number of nanoparticles present on the surface (Figure 7b) and shows that there are more cubic MNPs on the surface as indicated by the higher magnetic signal (Figure 7a) compared to that of the spherical MNPs. The data demonstrate that on applying the same force, a smaller number

DOI: 10.1021/acsomega.7b01312
ACS Omega 2017, 2, 8010−8019

of nanocubes (as compared to the nanospheres) were detached from the sensor surface. This preliminary study thereby validates our hypothesis that nanocubes provide a stronger binding to the sensor surface than that afforded by nanospheres.

We then used nanocubes and nanospheres with dissimilar volumes so we could compare the effect of applying the same centrifugal force to them (see Figures 7c and 7d). We compared three samples: (1) nanocubes with 135 nm side lengths, (2) nanocubes with 135 nm body-diagonal lengths, and (3) nanospheres with 135 nm diameters. Using FIRMS, we demonstrated that compared to nanospheres (135 nm diameter), a higher number of nanocubes (135 nm bd) remained on the surface, giving a higher signal after 7245*g* of centrifugal force. The higher magnetization and smaller mass of each 135 nm bd nanocube (and consequently, a higher number of these nanocubes as compared to 135 nm diameter nanospheres) can plausibly contribute to the higher magnetic response from the streptavidin-modified surface. We know that the centrifugal force experienced by any nanoparticle is directly proportional to its mass. Therefore, we further compared the 135 nm diameter nanospheres with the 135 nm side length nanocubes, which have higher volume and mass. The higher mass (10 fg) of each 135 nm side length nanocube as compared to each 135 nm diameter nanosphere (5 fg) corresponded to a lower number of cubic MNPs even though the total mass of the cubic and spherical MNP powder deposited on the surface was the same. Consequently, at the same rpm, the higher-volume (and higher-mass) nanocubes experienced a higher centrifugal force. Despite the relatively higher force experienced by the 135 nm side length nanocubes and their lower initial concentration (3.4×10^8 for 135 nm side length cubic, 1.6×10^9 for 135 nm body-diagonal length cubic, and 5.8×10^8 for spherical), compared to nanospheres, more 135 nm side length nanocubes remained on the surface after application of a force corresponding to 7245*g* (0.6 pN for 135 side length nanocubes, 0.1 pN for 135 nm body length diagonal nanocubes, and 0.4 pN for nanospheres). Figure 7d demonstrates that at 7245*g* centrifugal force (equivalent to 9000 rpm), the number of nanocubes (2.1×10^8) after removing nonspecific binding was almost three times as that of the nanospheres (0.7×10^8), even though the force experienced by each nanocube is almost twice that by each nanosphere. Both these studies unequivocally demonstrate that, because of their robust binding based on the higher contact area, the nanocubes require a much stronger force to break them away from the surface as compared to the nanospheres.

We have demonstrated that at a same-volume and a same-body diagonal/diameter basis, cubic Fe_3O_4 nanoparticles exhibit a higher magnetization and coercivity than their spherical counterparts in the 100−225 nm size range. The higher contact area of the nanocubes led to stronger attachment to the surface, which was demonstrated using FIRMS in all comparison studies (same volume, same-body diagonal/diameter, and same side length/diameter). We quantitatively showed that even when the initial number of (135 nm side length) nanocubes was an order of magnitude lower than that of (135 nm diameter) nanospheres, and force applied for nanocubes was 1.5 times that for nanospheres, a higher number of nanocubes remained on the surface, thus illustrating stronger binding and sensitivity potential of the nanocubes compared to the nanospheres. The enhanced magnetic properties and potentially higher sensing sensitivity of the nanocubes, as compared to the nanospheres, make nanocubes an attractive alternative to nanospheres in sensing applications.

CONCLUSIONS

The studies reported here allow us to conclude that, for sensing applications that rely on either a higher contact area or higher magnetization, higher crystallinity Fe_3O_4 nanocubes offer distinct advantages over polycrystalline Fe_3O_4 nanospheres of the same-volume or same-length diagonal or side length/diameter because of (1) stronger binding of nanocubes to substrate surfaces because of their greater contact area and (2) enhanced magnetic properties of the nanocubes due to their greater crystallinity in the multidomain size regime. Further work on synthesis of monocrystalline Fe_3O_4 spheres in this size regime (>80 nm diameter) is ongoing and will further delineate the relationships between nanoparticle shape, crystallinity, and magnetic properties.

EXPERIMENTAL SECTION

Nanoparticle Synthesis. We varied the reaction parameters in a modified thermal decomposition reaction[20,70] process and liquid-phase reduction process[47] to generate distinct sizes of Fe_3O_4 nanocubes and nanospheres. The chemicals used in the syntheses described below were of analytical grade and were used without further purification. Millipore water (resistivity higher than 18 MΩ cm) was used in the synthesis and washing steps.

Cubic Fe_3O_4 Synthesis. Using a variation of a known thermal decomposition method,[20,70] we synthesized Fe_3O_4 nanocubes with body-diagonal lengths of 135, 150, 175, and 225 nm (edge lengths 80, 85, 100, and 130 nm, respectively). Iron acetylacetonate [$Fe(acac)_3$] and oleic acid were heated to 290 °C in benzyl ether as a solvent and stirred in a round-bottomed flask using a magnetic stirrer. After 30 min, a black precipitate was obtained, which was washed multiple times with ethanol and dried under vacuum at room temperature. By varying the reactant concentration and reaction time, Fe_3O_4 nanocubes with tunable body-diagonal lengths were obtained.

Spherical Fe_3O_4 Synthesis. Our modified recipe of the procedure reported by Deng et al.[47] yielded spherical Fe_3O_4 nanoparticles with diameters of 100, 125, 135, 150, 175, and 275 nm. The procedure involved charging a round-bottomed flask with iron chloride (1.4 g, $FeCl_3{\cdot}6H_2O$) and 15 mL of ethylene glycol, followed sequentially by the addition of sodium acetate (3.6 g). The addition of sodium acetate rapidly turned the orange $FeCl_3{\cdot}6H_2O$ solution to a brown color. The solution was stirred for an additional 30 min and then injected at once into a round-bottomed flask containing a vigorously stirred solution of polyvinylpyrrolidone (0.40 g) in 35 mL of ethylene glycol heated to 180 °C. This mixture was then vigorously stirred at 180 °C for 4−24 h during which a black precipitate was obtained. The black precipitate was alternately washed multiple times with ethanol and Milli-Q water and dried under vacuum at room temperature. Agitation (stirrer speed), temperature, and reaction time were the process parameters that were varied to obtain Fe_3O_4 nanospheres of diameters that either matched the body diagonals of the synthesized nanocubes or had the same volume as that of the synthesized nanocubes.

Characterization. The nanoparticles were characterized by TEM (JEOL-2000 FX operating at 200 kV with attached energy dispersive X-ray spectroscopy), SEM (LEO-1525

DOI: 10.1021/acsomega.7b01312
ACS Omega 2017, 2, 8010−8019

operating at 15 kV), and XRD (Siemens D5000 X-ray diffractometer). For the TEM analyses, the nanoparticles were deposited on a 300-mesh holey carbon-coated copper grid and allowed to dry; for the SEM analyses, the nanoparticles were deposited on a silicon wafer and allowed to dry. The size distribution for each sample was generated by analysis of 50−60 nanoparticles. We used XRD for compositional and crystal structure confirmation. For analysis by XRD, a concentrated sample in ethanol was deposited on a piranha-cleaned glass slide, with XRD being carried out using Cu Kα radiation (λ = 1.540562 Å) at the 2θ range from 0° to 90°. In addition to imaging, TEM was also used to obtain diffraction patterns to obtain the crystallinity and compositional purity of the sample. The magnetic properties (saturation magnetization, residual magnetization, and coercivity) of a known mass of the sample were measured using a vibrating sample magnetometer (LakeShore VSM 7300 Series with LakeShore 735 Controller and LakeShore 450 Gaussmeter; Software Version 3.8.0). The Curie temperature data were obtained using VSM with varying-temperature capability (VSM PPMS EverCool II, Quantum Design, Inc., San Diego, CA, USA).

Preliminary Experiments Using a GMR Sensor. A basic giant magnetoresistive (GMR) sensor usually includes ferromagnetic layers interspersed with nonferromagnetic layers, and an antiferromagnetic exchange coupling generates the alternating opposing magnetization required for the GMR effect.[71] The magnetoresistance-based sensor (2 μm × 1.5 μm) used for our study consists of layers of Co/Cu/Co that are coated with alumina or silica. Aliquots of nanoparticles (same numbers of particles for each shape) were deposited on the sensors, which were then detected by a corresponding change in peak-to-peak distance (Δx as shown in Figure 6) on the plot of resistance versus field. In our preliminary experiments, we deposited 0.25 mL of 1 mg/mL (that is, the same number of same-volume cubic and spherical MNPs) on each sensor and noted the change in the peak-to-peak distance for each sample on each sensor. Additional details of sensor (production and SEM images) are supplied in the Supporting Information (Figure S2).

Preliminary Experiments Using FIRMS. In the FIRMS technique, a change in the magnetic signal is measured as a function of increasing mechanical force and was used to differentiate between the binding of the cubic and spherical MNPs to the sensor surface.[68] The MNPs were functionalized with biotin; the sensor surface was functionalized with streptavidin. Biotin-functionalized MNPs were well-dispersed in PBS buffer by shaker and incubated with the streptavidin-modified surface in a sample well for 2 h. Samples were magnetized by the application of a permanent magnet perpendicularly for 2 min at ∼0.5 T magnetic field before measurement. A mechanical force was applied to distinguish nonspecific versus specific ligand−receptor binding. A reduced magnetic signal due to the Brownian motion of the dissociated MNPs was used to randomize the magnetic dipoles. The remnant signal indicated the specific biotin−streptavidin binding. Measurements of the magnetic signals of the sample were obtained using an atomic magnetometer home-built in the Xu group.[72] The magnetic field generated from the MNPs was measured by the atomic magnetometer having a noise level of ∼1−2 pT in this work. The MNPs were allowed to bind to the surface and then subjected to centrifugation (centrifugal force), which removed unbound cubic and spherical MNPs from the surface. The functionalization of the MNPs and the sensor surface is described below.

Preparation of Biotin-Modified Magnetic Particles. To functionalize the magnetic particles with amino groups, the MNPs (0.003 g) were dispersed in 30 mL of ethanol solution in a 50 mL round-bottomed flask and sonicated for at least 30 min. To the well-dispersed MNP solution, we added 3-aminopropyltrimethoxysilane (0.2 mL) and then mechanically stirred the mixture overnight. The resulting particles were washed with ethanol and collected using centrifuge and magnetic separation several times. The amino-functionalized MNPs (0.5 mg) were dispersed in 300 μL of PBS buffer in a small glass vial for sonication (15 min). A mixture of 1.5 mg/100 μL biotin-PEG-SVA and 2 mg/100 μL mPEG-SVA was injected into the MNP dispersion. The reaction vial was shaken at 600 rpm for 4 h. The biotin-conjugated nanoparticles were washed with PBS buffer (pH 7.4) and isolated by magnetic separation several times, and then re-dispersed in PBS buffer with NaN_3 (0.2 w/w %).

Preparation of Streptavidin-Modified Surfaces. The streptavidin surfaces were prepared via layer-by-layer construction, which included an amino-functionalized layer, a biotinylated coating, and an outer streptavidin-terminated layer. One amino-functionalized slide was incubated with a mixture containing biotin-PEG-succinimidyl valerate and mPEG-succinimidyl valerate for 3 h. After biotinylation, all slides were rinsed with water and dried under a stream of nitrogen gas. The sample well was assembled by gluing the functionalized glass to a 20 × 3 × 1 mm^3 ($L \times W \times H$) piece of polystyrene having a 4 mm × 2 mm oval opening at the center (area ≈ 7 mm^2). The streptavidin surface was prepared through the conjugation between streptavidin and the biotin-modified surface, which was carried out by adding 8 μL of 0.625 mg/mL streptavidin into a sample well functionalized with biotin followed by incubation for 1 h.

■ ASSOCIATED CONTENT

Supporting Information

The Supporting Information is available free of charge on the ACS Publications website at DOI: 10.1021/acsomega.7b01312.

Information on the magnetic properties of nanoparticles of various shapes, additional data of crystallite sizes of synthesized MNPs, and details of the GMR sensor fabrication (PDF).

■ AUTHOR INFORMATION

Corresponding Authors

*E-mail: karen.martirosyan@utrgv.edu (K.S.M.).
*E-mail: litvinov@uh.edu (D.L.).
*E-mail: sxu7@central.uh.edu (S.X.).
*E-mail: willson@uh.edu (R.C.W).
*E-mail: trlee@uh.edu (T.R.L.).

ORCID

Dmitri Litvinov: 0000-0003-2272-562X
T. Randall Lee: 0000-0001-9584-8861

Author Contributions

R.C.W. and T.R.L. designed the project. A.G.K., Y.T.C., P.C., I.N., G.C.D., A.S., and I.A.R. performed the experiments and the characterizations. A.G.K., A.C.J., O.Z., I.A.R., K.M., D.L., S.J., R.C.W., and T.R.L. interpreted the data and wrote the paper. All authors discussed the results and commented on the manuscript.

DOI: 10.1021/acsomega.7b01312
ACS Omega 2017, 2, 8010−8019

Notes

The authors declare no competing financial interest.

■ ACKNOWLEDGMENTS

We thank the Asian Office of Aerospace Research and Development (AFOSR/AOARD FA2386-16-1-4067 to T.R.L.), the Robert A. Welch Foundation (E-1320 to T.R.L.), the Texas Center for Superconductivity (to T.R.L. and S.X.), the NIAID (1R21AI111120-01A1 to R.C.W.), and the National Science Foundation (CBET-1511789 to R.C.W. and ECCS-1508845 to S.X.) for supporting this research.

■ REFERENCES

(1) Tran, N.; Webster, T. J. Magnetic Nanoparticles: Biomedical Applications and Challenges. *J. Mater. Chem.* **2010**, *20*, 8760−8767.

(2) Roca, A. G.; Costo, R.; Rebolledo, A. F.; Veintemillas-Verdaguer, S.; Tartaj, P.; González-Carreño, T.; Morales, M. P.; Serna, C. J. Progress in the Preparation of Magnetic Nanoparticles for Applications in Biomedicine. *J. Phys. D: Appl. Phys.* **2009**, *42*, 224002.

(3) Thiesen, B.; Jordan, A. Clinical Applications of Magnetic Nanoparticles for Hyperthermia. *Int. J. Hyperthermia* **2008**, *24*, 467−474.

(4) Arruebo, M.; Fernández-Pacheco, R.; Ibarra, M. R.; Santamaría, J. Magnetic Nanoparticles for Drug Delivery. *Nano Today* **2007**, *2*, 22−32.

(5) Neuberger, T.; Schöpf, B.; Hofmann, H.; Hofmann, M.; Von Rechenberg, B. Superparamagnetic Nanoparticles for Biomedical Applications: Possibilities and Limitations of a New Drug Delivery System. *J. Magn. Magn. Mater.* **2005**, *293*, 483−496.

(6) Huang, S.-H.; Juang, R.-S. Biochemical and Biomedical Applications of Multifunctional Magnetic Nanoparticles: a Review. *J. Nanopart. Res.* **2011**, *13*, 4411−4430.

(7) Moerup, S.; Frandsen, C.; Hansen, M. F. *Magnetic Properties of Nanoparticles*; Oxford University Press, 2010; pp 713−744.

(8) Kolhatkar, A.; Jamison, A.; Litvinov, D.; Willson, R.; Lee, T. Tuning the Magnetic Properties of Nanoparticles. *Int. J. Mol. Sci.* **2013**, *14*, 15977−16009.

(9) Müller, R.; Dutz, S.; Neeb, A.; Cato, A. C. B.; Zeisberger, M. Magnetic Heating Effect of Nanoparticles with Different Sizes and Size Distributions. *J. Magn. Magn. Mater.* **2013**, *328*, 80−85.

(10) Caruntu, D.; Caruntu, G.; O'Connor, C. J. Magnetic Properties of Variable-Sized Fe_3O_4 Nanoparticles Synthesized from Non-Aqueous Homogeneous Solutions of Polyols. *J. Phys. D: Appl. Phys.* **2007**, *40*, 5801−5809.

(11) Guardia, P.; Labarta, A.; Batlle, X. Tuning the Size, the Shape, and the Magnetic Properties of Iron Oxide Nanoparticles. *J. Phys. Chem. C* **2011**, *115*, 390−396.

(12) Lu, H. M.; Zheng, W. T.; Jiang, Q. Saturation Magnetization of Ferromagnetic and Ferromagnetic Nanocrystals at Room Temperature. *J. Phys. D: Appl. Phys.* **2007**, *40*, 320−325.

(13) Chinnasamy, C.; Herr, J.; Pai, R.; Cui, B.; Li, W.; Liu, J. F. Gram Scale Synthesis of High Magnetic Moment $Fe_{100-x}Co_x$ Alloy Nanoparticles: Reaction Mechanism, Structural and Magnetic Properties and Its Application on Nanocomposite. *J. Appl. Phys.* **2012**, *111*, 07B539.

(14) Gabal, M. A.; Angari, A. Y. M.; Kadi, M. W. Structural and Magnetic Properties of Nanocrystalline $Ni_{1-x}Cu_xFe_2O_4$ Prepared through Oxalate Precursors. *Polyhedron* **2011**, *30*, 1185−1190.

(15) Kuhn, L. T.; Bojesen, A.; Timmermann, L.; Fauth, K.; Goering, E.; Johnson, E.; Nielson, M. M.; Mørup, S. Core-Shell Iron−Iron Oxide Nanoparticles: Magnetic Properties and Interactions. *J. Magn. Magn. Mater.* **2004**, *272*, 1485−1486.

(16) Luis, F.; Bartolomé, F.; Petroff, F.; Bartolomé, J.; García, L. M.; Deranlot, C.; Jaffrès, H.; Martínez, M. J.; Bencok, P.; Wilhelm, F.; Rogalev, A.; Brookes, N. B. Tuning the Magnetic Anisotropy of Co Nanoparticles by Metal Capping. *Europhys. Lett.* **2006**, *76*, 142−148.

(17) Singh, V.; Srinivas, V.; Ranot, M.; Angappane, S.; Park, J.-G. Effect of Polymer Coating on the Magnetic Properties of Oxygen-Stabilized Nickel Nanoparticles. *Phys. Rev. B: Condens. Matter Mater. Phys.* **2010**, *82*, 054417.

(18) Gao, G.; Liu, X.; Shi, R.; Zhou, K.; Shi, Y.; Ma, R.; Takayama-Muromachi, E.; Qiu, G. Shape-Controlled Synthesis and Magnetic Properties of Monodisperse Fe_3O_4 Nanocubes. *Cryst. Growth Des.* **2010**, *10*, 2888−2894.

(19) Leem, G.; Sarangi, S.; Zhang, S.; Rusakova, I.; Brazdeikis, A.; Litvinov, D.; Lee, T. R. Surfactant-Controlled Size and Shape Evolution of Magnetic Nanoparticles. *Cryst. Growth Des.* **2009**, *9*, 32−34.

(20) Kim, D.; Lee, N.; Park, M.; Kim, B. H.; An, K.; Hyeon, T. Synthesis of Uniform Ferrimagnetic Magnetite Nanocubes. *J. Am. Chem. Soc.* **2009**, *131*, 454−455.

(21) Yan, M.; Fresnais, J.; Berret, J.-F. Growth Mechanism of Nanostructured Superparamagnetic Rods Obtained by Electrostatic Co-Assembly. *Soft Matter* **2010**, *6*, 1997−2005.

(22) Wu, C.-G.; Lin, H. L.; Shau, N.-L. Magnetic Nanowires via Template Electrodeposition. *J. Solid State Electrochem.* **2006**, *10*, 198−202.

(23) Srikala, D.; Singh, V. N.; Banerjee, A.; Mehta, B. R.; Patnaik, S. Synthesis and Characterization of Ferromagnetic Cobalt Nanospheres, Nanodiscs and Nanocubes. *J. Nanosci. Nanotechnol.* **2009**, *9*, 5627−5632.

(24) Comesaña-Hermo, M.; Ciuculescu, D.; Li, Z.-A.; Stienen, S.; Spasova, M.; Farle, M.; Amiens, C. Stable Single Domain Co Nanodisks. Synthesis, Structure and Magnetism. *J. Mater. Chem.* **2012**, *22*, 8043−8047.

(25) Schladt, T. D.; Shukoor, M. I.; Schneider, K.; Tahir, M. N.; Natalio, F.; Ament, I.; Becker, J.; Jochum, F. D.; Weber, S.; Köhler, O.; Theato, P.; Schreiber, L. M.; Sönnichsen, C.; Schröder, H. C.; Müller, W. E. G.; Tremel, W. Au@MnO Nanoflowers: Hybrid Nanocomposites for Selective Dual Functionalization and Imaging. *Angew. Chem., Int. Ed.* **2010**, *49*, 3976−3980.

(26) Dovgolevsky, E.; Haick, H. Direct Observation of the Transition Point between Quasi-Spherical and Cubic Nanoparticles in a Two-Step Seed-Mediated Growth Method. *Small* **2008**, *4*, 2059−2066.

(27) He, X.; Shi, H. Size and Shape Effects on Magnetic properties of Ni Nanoparticles. *Particuology* **2012**, *10*, 497−502.

(28) de Montferrand, C.; Hu, L.; Milosevic, I.; Russier, V.; Bonnin, D.; Motte, L.; Brioude, A.; Lalatonne, Y. Iron Oxide Nanoparticles with Sizes, Shapes and Compositions Resulting in Different Magnetization Signatures as Potential Labels for Multiparametric Detection. *Acta Biomater.* **2013**, *9*, 6150−6157.

(29) Song, Q.; Zhang, Z. J. Shape Control and Associated Magnetic Properties of Spinel Cobalt Ferrite Nanocrystals. *J. Am. Chem. Soc.* **2004**, *126*, 6164−6168.

(30) Salazar-Alvarez, G.; Qin, J.; Šepelák, V.; Bergmann, I.; Vasilakaki, M.; Trohidou, K. N.; Ardisson, J. D.; Macedo, W. A. A.; Mikhaylova, M.; Muhammed, M.; Baró, M. D.; Nogués, J. Cubic Versus Spherical Magnetic Nanoparticles: The Role of Surface Anisotropy. *J. Am. Chem. Soc.* **2008**, *130*, 13234−13239.

(31) Zhen, G.; Muir, B. W.; Moffat, B. A.; Harbour, P.; Murray, K. S.; Moubaraki, B.; Suzuki, K.; Madsen, I.; Agron-Olshina, N.; Waddington, L.; Mulvaney, P.; Hartley, P. G. Comparative Study of the Magnetic Behavior of Spherical and Cubic Superparamagnetic Iron Oxide Nanoparticles. *J. Phys. Chem. C* **2011**, *115*, 327−334.

(32) Chou, S.-W.; Zhu, C.-L.; Neeleshwar, S.; Chen, C.-L.; Chen, Y.-Y.; Chen, C.-C. Controlled Growth and Magnetic Property of FePt Nanostructure: Cuboctahedron, Octapod, Truncated Cube, and Cube. *Chem. Mater.* **2009**, *21*, 4955−4961.

(33) Liu, Y.; Tan, J.; Thomas, A.; Ou-Yang, D.; Muzykantov, V. R. The Shape of Things to Come: Importance of Design in Nanotechnology for Drug Delivery. *Ther. Delivery* **2012**, *3*, 181−194.

(34) Decuzzi, P.; Ferrari, M. The Adhesive Strength of Non-Spherical Particles Mediated by Specific Interactions. *Biomaterials* **2006**, *27*, 5307−5314.

(35) Decuzzi, P.; Pasqualini, R.; Arap, W.; Ferrari, M. Intravascular Delivery of Particulate Systems: Does Geometry Really Matter? *Pharm. Res.* **2009**, *26*, 235−243.

DOI: 10.1021/acsomega.7b01312
ACS Omega 2017, 2, 8010−8019

(36) Shah, S.; Liu, Y.; Hu, W.; Gao, J. Modeling Particle Shape-Dependent Dynamics in Nanomedicine. *J. Nanosci. Nanotechnol.* **2011**, *11*, 919−928.
(37) Gentile, F.; Chiappini, C.; Fine, D.; Bhavane, R. C.; Peluccio, M. S.; Cheng, M. M.-C.; Liu, X.; Ferrari, M.; Decuzzi, P. The Effect of Shape on the Margination Dynamics of Non-Neutrally Buoyant Particles in Two-Dimensional Shear Flows. *J. Biomech.* **2008**, *41*, 2312−2318.
(38) Decuzzi, P.; Godin, B.; Tanaka, T.; Lee, S.-Y.; Chiappini, C.; Liu, X.; Ferrari, M. Size and Shape Effects in the Biodistribution of Intravascularly Injected Particles. *J. Controlled Release* **2010**, *141*, 320−327.
(39) Blanco, E.; Shen, H.; Ferrari, M. Principles of Nanoparticle Design for Overcoming biological Barriers to Drug Delivery. *Nat. Biotechnol.* **2015**, *33*, 941−951.
(40) Kolhatkar, A. G.; Nekrashevich, I.; Litvinov, D.; Willson, R. C.; Lee, T. R. Cubic Silica-Coated and Amine-Functionalized FeCo Nanoparticles with High Saturation Magnetization. *Chem. Mater.* **2013**, *25*, 1092−1097.
(41) Noh, S.-h.; Na, W.; Jang, J.-t.; Lee, J.-H.; Lee, E. J.; Moon, S. H.; Lim, Y.; Shin, J.-S.; Cheon, J. Nanoscale Magnetism Control via Surface and Exchange Anisotropy for Optimized Ferrimagnetic Hysteresis. *Nano Lett.* **2012**, *12*, 3716−3721.
(42) Jović, N.; Prekajski, M.; Kremenović, A.; Jančar, B.; Kahlenberg, V.; Antić, B. Influence of Size/Crystallinity Effects on the Cation Ordering and Magnetism of α-Lithium Ferrite Nanoparticles. *J. Appl. Phys.* **2012**, *111*, 034313.
(43) Chia, C. H.; Zakaria, S.; Yusoff, M.; Goh, S. C.; Haw, C. Y.; Ahmadi, S.; Huang, N. M.; Lim, H. N. Size and Crystallinity-Dependent Magnetic Properties of $CoFe_2O_4$ Nanocrystals. *Ceram. Int.* **2010**, *36*, 605−609.
(44) Mozaffari, M.; Manouchehri, S.; Yousefi, M. H.; Amighian, J. The Effect of Solution Temperature on Crystallite Size and Magnetic Properties of Zn Substituted Co Ferrite Nanoparticles. *J. Magn. Magn. Mater.* **2010**, *322*, 383−388.
(45) Deraz, N. M. Size and Crystallinity-Dependent Magnetic Properties of Copper Ferrite Nano-Particles. *J. Alloys Compd.* **2010**, *501*, 317−325.
(46) Jeong, U.; Teng, X.; Wang, Y.; Yang, H.; Xia, Y. Superparamagnetic Colloids: Controlled Synthesis and Niche Applications. *Adv. Mater.* **2007**, *19*, 33−60.
(47) Deng, H.; Li, X.; Peng, Q.; Wang, X.; Chen, J.; Li, Y. Monodisperse Magnetic Single-Crystal Ferrite Microspheres. *Angew. Chem., Int. Ed.* **2005**, *44*, 2782−2785.
(48) Köse, H.; Aydin, A. O.; Akbulut, H. The Effect of Temperature on Grain Size of SnO_2 Nanoparticles Synthesized by Sol-Gel Method. *Acta Phys. Pol., A* **2014**, *125*, 345−347.
(49) Sahai, A.; Goswami, N. Structural and Vibrational Properties of ZnO Nanoparticles Synthesized by the Chemical Precipitation Method. *Phys. E* **2014**, *58*, 130−137.
(50) Liu, Y.; Cui, T.; Li, Y.; Zhao, Y.; Ye, Y.; Wu, W.; Tong, G. Effects of Crystal Size and Sphere Diameter on Static Magnetic and Electromagnetic Properties of Monodisperse Fe_3O_4 Microspheres. *Mater. Chem. Phys.* **2016**, *173*, 152−160.
(51) Kolhatkar, A.; Jamison, A.; Litvinov, D.; Willson, R.; Lee, T. Tuning the Magnetic Properties of Nanoparticles. *Int. J. Mol. Sci.* **2013**, *14*, 15977−16009.
(52) Baselt, D. R.; Lee, G. U.; Natesan, M.; Metzger, S. W.; Sheehan, P. E.; Colton, R. J. A Biosensor Based on Magnetoresistance Technology. *Biosens. Bioelectron.* **1998**, *13*, 731−739.
(53) Reiss, G.; Brueckl, H.; Huetten, A.; Schotter, J.; Brzeska, M.; Panhorst, M.; Sudfeld, D.; Becker, A.; Kamp, P. B.; Puehler, A.; Wojczykowski, K.; Jutzi, P. Magnetoresistive Sensors and Magnetic Nanoparticles for Biotechnology. *J. Mater. Res.* **2005**, *12*, 3294−3302.
(54) Hall, D. A.; Gaster, R. S.; Osterfeld, S. J.; Murmann, B.; Wang, S. X. GMR Biosensor Arrays: Correction Techniques for Reproducibility and Enhanced Sensitivity. *Biosens. Bioelectron.* **2010**, *25*, 2177−2181.
(55) Hall, D. A.; Wang, S. X.; Murmann, B.; Gaster, R. S. Portable Biomarker Detection with Magnetic Nanotags. *Proceedings of 2010 IEEE International Symposium on Circuits and Systems*, 2010; pp 1779−1782.
(56) Hall, D. A.; Gaster, R. S.; Lin, T.; Osterfeld, S. J.; Han, S.; Murmann, B.; Wang, S. X. GMR Biosensor Arrays: A System Perspective. *Biosens. Bioelectron.* **2010**, *25*, 2051−2057.
(57) Gaster, R. S.; Hall, D. A.; Nielsen, C. H.; Osterfeld, S. J.; Yu, H.; Mach, K. E.; Wilson, R. J.; Murmann, B.; Liao, J. C.; Gambhir, S. S.; Wang, S. X. Matrix-Insensitive Protein Assays Push the Limits of Biosensors in Medicine. *Nat. Med.* **2009**, *15*, 1327−1332.
(58) Osterfeld, S. J.; Yu, H.; Gaster, R. S.; Caramuta, S.; Xu, L.; Han, S.-J.; Hall, D. A.; Wilson, R. J.; Sun, S.; White, R. L.; Davis, R. W.; Pourmand, N.; Wang, S. X. Multiplex Protein Assay Based on Real-Time Magnetic Nanotag Sensing. *Proc. Natl. Acad. Sci. U.S.A.* **2008**, *105*, 20637−20640.
(59) Ferreira, H. A.; Graham, D. L.; Freitas, P. P.; Cabral, J. M. S. Biodetection Using Magnetically Labeled Biomolecules and Arrays of Spin Valve Sensors. *J. Appl. Phys.* **2003**, *93*, 7281−7286.
(60) Rife, J. C.; Miller, M. M.; Sheehan, P. E.; Tamanaha, C. R.; Tondra, M.; Whitman, L. J. Design and Performance of GMR Sensors for the Detection of Magnetic Microbeads in Biosensors. *Sens. Actuators, A* **2003**, *107*, 209−218.
(61) Edelstein, R. L.; Tamanaha, C. R.; Sheehan, P. E.; Miller, M. M.; Baselt, D. R.; Whitman, L. J.; Colton, R. J. The BARC Biosensor Applied to the Detection of Biological Warfare Agents. *Biosens. Bioelectron.* **2000**, *14*, 805−813.
(62) Schotter, J.; Kamp, P. B.; Becker, A.; Pühler, A.; Reiss, G.; Brückl, H. Comparison of a Prototype Magnetoresistive Biosensor to Standard Fluorescent DNA Detection. *Biosens. Bioelectron.* **2004**, *19*, 1149−1156.
(63) Chen, C.; Suzuki, Y.; Kato, T.; Iwata, S.; Tsunashima, S.; Toyoda, H.; Sugai, H. Dependences of Giant Magnetoresistance in Co/Cu Multilayers on Sputtering Conditions. *Jpn. J. Appl. Phys., Part 1* **2006**, *45*, 8466−8468.
(64) Chapman, J. N.; Rose, J.; Aitchison, P. R.; Holloway, H.; Kubinski, D. J. Magnetization Processes in Co/Cu Multilayers with Low Magnetoresistive Hysteresis. *J. Appl. Phys.* **1999**, *86*, 1611−1620.
(65) Xu, L.; Yu, H.; Akhras, M. S.; Han, S.-J.; Osterfeld, S.; White, R. L.; Pourmand, N.; Wang, S. X. Giant Magnetoresistive Biochip for DNA Detection and HPV Genotyping. *Biosens. Bioelectron.* **2008**, *24*, 99−103.
(66) Sakai, T.; Oomi, G.; Okada, K.; Takanashi, K.; Saito, K.; Fujimori, H. Difference between the Giant Magnetoresistance of Fe/Cu and Co/Cu Magnetic Multilayers under High Pressure. *Phys. B* **1997**, *239*, 53−55.
(67) Miyazaki, T.; Tezuka, N. Giant Magnetic Tunneling Effect in $Fe/Al_2O_3/Fe$ Junction. *J. Magn. Magn. Mater.* **1995**, *139*, L231−L234.
(68) Yao, L.; Xu, S. Force-Induced Remnant Magnetization Spectroscopy for Specific Magnetic Imaging of Molecules. *Angew. Chem., Int. Ed.* **2011**, *50*, 4407−4409.
(69) Chen, Y.-T.; Jamison, A. C.; Lee, T. R.; Xu, S. Quantitatively Resolving Ligand−Receptor Bonds on Cell Surfaces Using Force-Induced Remnant Magnetization Spectroscopy. *ACS Cent. Sci.* **2016**, *2*, 75−79.
(70) Yang, H.; Ogawa, T.; Hasegawa, D.; Takahashi, M. Synthesis and Magnetic Properties of Monodisperse Magnetite Nanocubes. *J. Appl. Phys.* **2008**, *103*, 07D526.
(71) Litvinov, D.; Willson, R.; Wolfe, J. C. Nanomagnetic Detector Array for Biomolecular Recognition. WO2007014322 A2, 2007.
(72) Yao, L.; Xu, S. Long-Range, High-Resolution Magnetic Imaging of Nanoparticles. *Angew. Chem., Int. Ed.* **2009**, *48*, 5679−5682.

DOI: 10.1021/acsomega.7b01312
ACS Omega 2017, 2, 8010−8019